https://doi.org/10.5194/bg-2021-332
Preprint. Discussion started: 21 December 2021

Biogeosciences Discussions
Open Access
EGU

Fossilization of Precambrian microfossils in the Volyn pegmatite, Ukraine

Gerhard Franz[1], Peter Lyckberg[2], Vladimir Khomenko[3], Vsevolod Chournousenko[4], Hans-Martin Schulz[5], Nicolaj Mahlstedt[5], Richard Wirth[5], Johannes Glodny[5], Uli Gernert[6], Jörg Nissen[6]

[1]Institut für Angewandte Geowissenschaften, Technische Universität Berlin, D-10587 Berlin, Germany

[2]Luxembourg National Museum of Natural History, 25 Rue Münster, 2160 Luxembourg, Luxembourg

[3]The National Academy of Sciences of Ukraine, M.P. Semenenko Institute of Geochemistry, Mineralogy and Ore Formation, 34, Palladina av., Kyiv, 03142, Ukraine

[4]Volyn Quartz Samotsvety Company, Khoroshiv (Volodarsk-Volynski), Ukraine

[5]GFZ German Research Centre for Geosciences, Telegrafenberg, D-14473 Potsdam, Germany

[6]Zentraleinrichtung Elektronenmikroskopie, Technische Universität Berlin, D-10623 Berlin, Germany

Corresponding author: Gerhard Franz; e-mail: gefra548@gmail.com

https://doi.org/10.5194/bg-2021-332
Preprint. Discussion started: 21 December 2021


Biogeosciences Discussions

Abstract

We report on Precambrian soft-tissue microfossils from igneous rocks of the Volyn pegmatite district, associated with the Paleoproterozoic Korosten Pluton, north-western Ukraine. The fossils were recovered from m-sized miarolitic cavities and show a well-preserved 3D morphology, mostly fibrous, but with a large variety of fiber types, and also in irregular, flaky shapes reminiscent of former biofilms, and rare spherical objects. Based on literature data, own pyrolysis experiments and reflected light microscopy results, the organic matter (OM) is characterized as (oxy)kerite. Further investigations with microscopic techniques, including scanning and transmission electron microscopy, and electron microprobe analysis show that fossilization likely occurred during a hydrothermal, post-pegmatitic event, by silicification dominantly in the outermost 1-2 µm of the microfossils. The hydrothermal fluid, derived from the pegmatitic environment, was enriched in SiF_4, Al, Ca, Na, K, Cl, and S. The OM shows O enrichment where N and S content is low, indicating simultaneous N and S loss during anaerobic oxidation. Mineralization with Al-silicates starts at the rim of the microfossils, continues in its outer parts into identifiable encrustations and intergrowths of clay minerals, feldspar, Ca-sulfate, Ca-phosphate, Fe-sulfide, and fluorite.

Breccias, formed during collapse of some the miarolitic cavities, contain also decaying OM, which released high concentrations of dissolved NH_4^+, responsible for the late-stage formation of buddingtonite and tobelite-rich muscovite. The age of the fossils can be restricted to the time between the pegmatite formation, at ~1.760 Ga, and the breccia formation at ~ 1.49 Ga. As geological environment for growth of the microorganisms and fossilization we assume a geyser system, in which the essential biological components C, N, S, and P for growth of the organisms in the miarolitic caves were derived from microorganisms at the surface. Fossilization was induced by magmatic SiF_4-rich fluids. The Volyn occurrence is a prime example of

https://doi.org/10.5194/bg-2021-332
Preprint. Discussion started: 21 December 2021

44 Precambrian fossils and the results underline the importance of cavities in granitic rocks as a
45 possible habitat for microorganisms of the deep biosphere.

46

47 Key words: microfossils, fossilization, Precambrian, pegmatite, deep biosphere

https://doi.org/10.5194/bg-2021-332
Preprint. Discussion started: 21 December 2021

1. Introduction

Precambrian soft-tissue fossils are generally rare and their morphology is generally not well preserved. They occur mostly in (meta)sediments, but in recent years it became evident that also pores, fissures and other open spaces in igneous rocks can be a habitat for microorganisms. In miarolitic cavities in pegmatites from the Volyn pegmatite district, Ukraine, genetically associated with the Paleoproterozoic Korosten pluton of the western Ukrainian shield (Fig. 1), organic matter (OM) occurs in a conspicuous fibrous form. It is known as 'kerite' and was first described by Ginzburg et al. (1987) as a result of abiogenic sublimation and polymerization of volatile hydrocarbons from the pegmatite. In Ukrainian-Russian literature the OM was characterized as (oxy)kerite, i.e. highly mature OM. Gorlenko et al. (2000) and Zhmur (2003) were the first to re-interpret these kerites as fossils of filamentous cyanobacteria, based on electron microscopic investigations on ultra-thin sections. They also pointed out that cyanobacteria are not the only microorganisms, but they described the occurrence as a microbial community, an 'Early Proterozoic autonomous biocoenosis'. Stable $\delta^{13}C$ isotope ratios ≤40 ‰ of such fibers are similar to $\delta^{13}C$ isotope ratios in methanogenic bacteria (Franz et al. 2017). Typical for the OM is the high N-content, which goes up to 9 wt% (Luk'yanova et al., 1992; Franz et al., 2017). The maximum age of the fossils is restricted by the 1760±3 Ma intrusion age of the pegmatites (Shumlyanskyy et al., 2021; Fig. 1). The minimum age is constrained by ^{40}Ar-^{39}Ar laser-ablation age data of minerals in a breccia, which formed after consolidation of the pegmatites. This breccia contains degraded OM together with newly formed muscovite (formation age 1491±9 Ma; Franz et al., in review) and buddingtonite, NH_4-feldspar (minimum age of 563±14 Ma). Ammonium ions are a product of the degradation of OM, and the white mica age and the buddingtonite age restrict the age of the organisms most likely near to 1.5 Ga, the age of pseudomorph formation (for detailed discussion see Franz et al., in press). (*Footnote: In the title of Zhmur, 2003, there is an obvious typing error: It says "Origin of Cambrian fibrous*

https://doi.org/10.5194/bg-2021-332
Preprint. Discussion started: 21 December 2021

kerites of the Volyn region", but in the text it is clear that the authors refer to a Precambrian age.)

The miarolitic cavities hosting the kerite fossils are a special feature of these pegmatites, which are therefore referred to as 'chamber pegmatites' (see reviews in Ivanovich and Alekseevich, 2007; Lyckberg et al., 2009). These chambers are zones of free growth for crystals ('crystal pockets') and were formed in the cooling stage of the pegmatite, in the same way as common miarolitic cavities, i.e. from magmatic fluids, liberated during crystallization. What is unusual is their size: Lyckberg et al. (2019) describe the largest pocket of pegmatite no. 521 in a depth of 96 m with dimensions of 45 m in length, up to 25 m wide and about 20 m high. Common are cavity dimensions of 4 to 6 m in length, 3 to 4 m wide, and 1 to 3 m high (Ivanov and Alekseevich, 2007), and the unusually large size is attributed to the long cooling history of the Korosten pluton with supply of fluids from anorthositic magmas (Shumlyanskyy et al., 2021).

A striking feature of the OM is the well-preserved morphology (Zhmur, 2003; Franz et al., 2017), which poses the question how the delicate OM without skeletal parts in the organisms was fossilized. Zhmur (2003) interpreted this process as 'hydrocarbon-aqueous fossilization' due to prolonged low-temperature dehydration and oxidation. Here we present data from reflected light microscopy, scanning electron microscopy (SEM), transmission electron microscopy (TEM), and electron probe microanalysis (EMPA) to show that the fossilization process is mainly driven by the reaction of Si-Al-(Ca) with the OM via a fluid phase rich in F, Cl, S, and P, followed by encrustation of Al-silicates. Results of open-system pyrolysis and TEM show that the OM is highly mature, but still completely amorphous. Attempts to date the fibrous kerite directly, and of opal with inclusions of OM with $^{207}Pb/^{204}Pb$ vs $^{206}Pb/^{204}Pb$ partly failed, but are consistent with the inferred Precambrian age.

https://doi.org/10.5194/bg-2021-332
Preprint. Discussion started: 21 December 2021

Biogeosciences
Discussions
Open Access
EGU

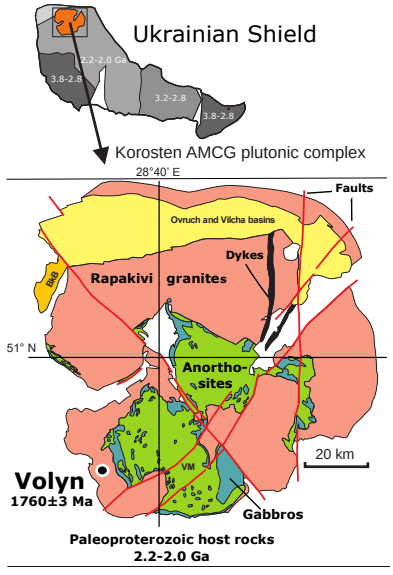

Figure 1: Location of the Volyn pegmatite field (asterisk) in the Korosten anorthosite-mangerite-charnockite-granite plutonic complex, north-western Ukrainian Shield (numbers refer to the ages in Ga of consolidation of the shield; Shumlyanskyy et al., 2017). The pegmatite age of 1760±3 Ma at Volyn refers to zircon U-Pb SIMS data (Shumlyanskyy et al., 2021).

1.1 Sample material and methods

Sample material from the Volyn pegmatite includes kerite, obtained from the Museum of the National Academy of Sciences, Semenenko Institute of Geochemistry, Mineralogy and Ore Formation, Kyiv, and seven kerite samples, sampled in situ from the pegmatites (Table 1). In addition, we investigated single crystals of beryl with etch pits, which contain OM, and use data from a previously investigated sample 2008-V (Franz et al., 2017), a breccia collected from the mine tailings of pegmatite no. 2, which contains degraded OM in a pseudomorph after beryl, consisting of buddingtonite, muscovite, betrandite, and opal. For the age determination, we used this OM together with sample #9 (Table 1; aliquots a,b,c), which is topaz with degraded OM, and black opal (sample BO, subdivided into aliquots) from the same shaft.

https://doi.org/10.5194/bg-2021-332
Preprint. Discussion started: 21 December 2021

115 Table 1: List of samples and their macroscopic appearance

No./GFZ no.	Year of sampling	Material	Location	Morphology
0/Museum Ac. Sci. Kyiv	unknown	kerite	unknown	fibrous
1/G017809	2018	kerite	shaft 3	fibrous
2/G017810	2018	kerite	shaft 3	fibrous
3/G017811	2018	kerite	shaft 3	fibrous
4/G017812	2018	kerite	shaft 3	fibrous, spherical
5/G017813	2013	kerite	shaft 3	irregular, botryoidal
6/G017814	2013	kerite	shaft 3	fibrous, irregular
7/G017815	2013	kerite	shaft 3	fibrous, spherical
2008-V-10	2008	beryl crystal with etch pits	mine tailings pegmatite #2	fibrous, spherical, irregular
9a,b,c	2018	topaz with OM	shaft 3	(degraded OM)
BO	2018	black opal	shaft 3	(inclusions of OM)
2008-V-1,a,b,c	2008	pseudomorph after beryl	mine tailings pegmatite #2	(degraded OM)

116

117 SEM images were obtained with a Hitachi SU8030 instrument, equipped with an EDAX EDS
118 system with a 30 mm^2 silicon drift detector (SDD) fitted with a silicon nitride window. We first
119 tried to work without coating but the fibers are non-conductive and were electrically charged.
120 Samples were therefore coated with an approximately 5 nm thick Ir layer allowing for high-
121 resolution imaging of the fiber surfaces without a structure of the commonly applied Au
122 coating. The kerite fibers without further cleaning or preparation were mounted on Al stubs
123 stickered with conductive carbon tabs.

124 The JEOL JXA-8530F field emission microprobe at TU Berlin was used to investigate the same
125 mounts that were used for reflected light microscopy, but with C-coating, for quantitative
126 results and less absorbance (compared to Ir). EPMA data for mapping were acquired using an
127 8 kV, 20 nA beam with a probe diameter of 64 nm. Cross sections of the fibers or parts of the
128 rim of OM were selected for mapping of element distribution in the wave-length dispersive
129 mode of the microprobe. Mappings were made in stage scan-modus with pixel resolution
130 between 277 and 360 x 180 and 265, with a pixel size of mostly 80 nm, and a dwell time per
131 pixel of 200 ms. Total scan areas varied between 70 x 36 µm to 33.2 x 31.8 µm.

https://doi.org/10.5194/bg-2021-332
Preprint. Discussion started: 21 December 2021

Open-system pyrolysis was performed using a Quantum MSSV-2 Thermal Analyzer© interfaced with an Agilent GC 6890A gas chromatograph. Milligram quantities (0.3-2.0 mg) of freshly powdered sample material were weighed into the central part of small glass capillaries and fixed with purified quartz wool that had been cleaned by heating at 630°C in air for 30 min. Open-system pyrolysis was performed from 300°C to 600°C at 40°C/min in a flow of He at a rate of 30 mL/min. The generated hydrocarbons were immediately transferred to a liquid nitrogen cooled trap and subsequently analyzed using an Agilent GC 6890A gas chromatograph equipped with an HP-Ultra 1 column of 50 m length, 50m x 32mm internal diameter, dimethylpolysiloxane-coated column (0.52 µm film thickness), and flame ionization detector. The oven temperature was programmed from 30°C to 320°C at 5°C/min. Qualification of single compounds was conducted using reference chromatograms.

For the U-Th-Pb analysis, fragments of OM from two samples were selected under a binocular microscope. Fragments from sample No. 9 were visually pure, inclusion-free, with a dark brownish color. Fragments from sample No. 1 showed fine-grained intergrowth with colorless to whitish phases, probably quartz and feldspar. After cleaning in double-distilled water in an ultrasonic bath, fragments (weight between 0.38 and 2.53 mg) were digested in conc. HNO_3 at 220°C for 48 h using a Parr-type hydrothermal digestion vessel. Careful optical control revealed that all organic material was fully dissolved in this step. Sample solutions were dried and re-dissolved in 2%-HNO_3. Concentrations of U and Th were measured by isotope dilution on a Thermo Scientific ELEMENT XR ICP-MS at GFZ Potsdam, using a mixed ^{235}U-^{230}Th spike. Concentrations of lead isotopes ^{204}Pb, ^{206}Pb, ^{207}Pb, and ^{208}Pb were determined on the same instrument from sample signal count rates compared to an external calibration curve for Pb. Corrections for background and for interference of ^{204}Hg on the ^{204}Pb signal were applied.

2 Results

2.1 SEM images

https://doi.org/10.5194/bg-2021-332
Preprint. Discussion started: 21 December 2021


Biogeosciences
Discussions
Open Access
EGU

157 The morphology of the OM is best illustrated in SEM images (Fig. 2). There are three different
158 types of morphologies, classified as fibrous, often branched (Fig. 2a,c), as spherical (Fig. 2b),
159 and irregular, flaky objects (Fig. 2c). Objects with spherical morphology are rare, therefore we
160 restrict to the fibers and flakes, which could also be found in thick sections of OM embedded
161 in epoxy, and thus available for more detailed analytical investigations. Fibers are the dominant
162 form. Broken pieces are up to ~1 cm long and have a variable diameter, from 1-2 µm up to c.
163 80 µm, mostly near c. 15-20 µm. Many of the fibers are branched (Fig. 2d), or segmented (Fig.
164 2e,f) and show globular outgrowths, some of these outgrowths with botryoidal shape (Fig. 2e).
165 This botryoidal shape can extend into more irregular, ridged forms. Flaky OM is best seen in
166 etch pits of beryl from Volyn (Fig. 2a,c), attached together with fibrous and rare spherical
167 objects to the surface of beryl.

168 In many cases we see minerals grown onto the fibers, identified by chemical composition and
169 shape as e.g. kaolinite and chlorite (Fig. 3a), illite and Na-Al-silicate (Fig. 3b); for
170 documentation of the EDS spectra see Fig. SI1 Supplementary Information. On fibers with a
171 rather smooth surface we see structures in the order of 100 x 500 nm which are enriched in Al,
172 Si, Fe, and S, probably pyrite/markasite with Si-Al-incrustations (Fig. 3c). Segmented fibers
173 (Fig. 3d) show larger structures and the EDS analysis indicates incrustations of clay minerals
174 such as illite/kaolinite. In many spectra, the peak of Ir is relatively broad and this might be an
175 indication for overlapping with a P-peak. As we show later (results of EMPA), P is indeed
176 present in the rims of the OM. The matrix between fibers consists of opal, intergrown with
177 silicates, probably Na-feldspar, and clay minerals (Fig. 3e,f). In several cases, fluorite crystals
178 could be identified together with the incrustations. In this case, there are also traces of Ca in the
179 incrustation.

180

https://doi.org/10.5194/bg-2021-332
Preprint. Discussion started: 21 December 2021

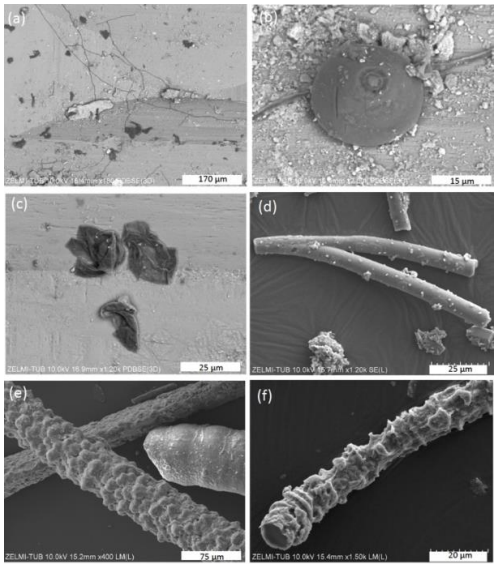

Figure 2: SEM images of kerite fossils, illustrating the different morphologies. (a) Fibrous and flaky OM in etch pits of beryl (sample #10). (b) Spherical object on a fiber (sample #10). (c) Flaky OM (sample #10). (d) Branched fiber with smooth surface (sample #4). (e) Fibers with a botryoidal and a smooth, slightly segmented surface (sample #5). (f) Fiber with a strongly segmented surface (sample #2).

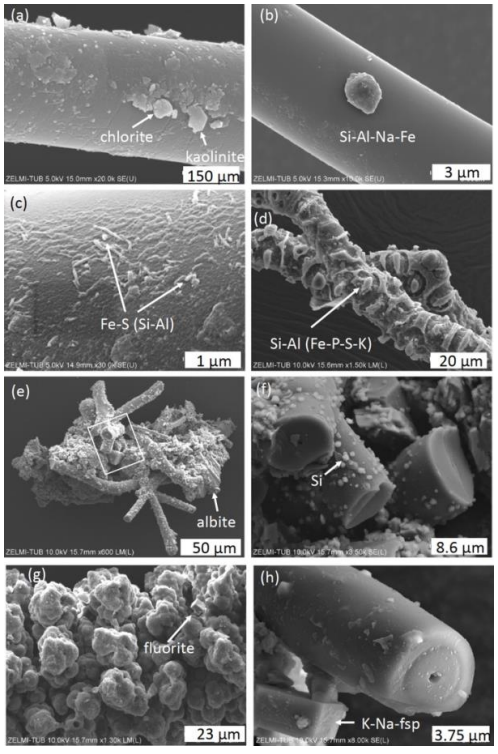

https://doi.org/10.5194/bg-2021-332
Preprint. Discussion started: 21 December 2021

Figure 3: SEM images of minerals, associated with OM. (a) Chlorite and kaolinite, and (b) unidentified Na-Fe-Al-silicate grain grown onto a fiber (sample #0). (c) High-magnification of fiber surface with Fe-sulfide (pyrite/markasite?) and incrustations of Si-Al (sample #0). (d) Incrustation on segmented fiber, with dominantly Si-Al, minor peaks of Fe-P-S-K (sample #4). (e) Aggregate of fibers, cemented by minerals; lower right is an albite crystal; rectangle shows position of (f), enlarged part with broken fibers and small opal grains (identified by a Si-peak and globular shape) attached to the surface (sample #4). (g) Aggregates forming a botryoidal surface of a fiber, intergrown with a fluorite crystal. (h) Alkalifeldspar, grown onto a broken fiber with central cavity.

The surface of botryoidal shapes (Fig. 4a) shows µm-wide gaps, explained as shrinking cracks, and ball-shaped outgrowths (Fig. 4b,c) with a dented surface, interpreted as a result of degassing of the OM. The EDS-spectra of the surface shows peaks for Al and Si, in addition to the C-N-O-content of the OM. The internal structure of the OM is seen in a broken face of a fiber; it is characterized by a porosity (Fig. 4e-h), also interpreted as result of degassing. Individual pores are irregular in shape and in the order of several 100 nm large (Fig. 4g,h). Some of the broken fibers show in their cross section a central cavity, i.e. a channel extending along the fiber axis (Figs. 3h, 5). The cross sections of this channel vary from c. 250 x 500 nm (Fig. 5a) to c. 20 x 20 µm (Fig. 5f) in diameter. In some cases, the channel has a six-sided outline (Fig. 5f,g,h). The fractured surface with fringe fractures, sub-perpendicular to the fiber length (Fig. 5a,g), indicates brittle behavior of the fibers, which was also observed during handling the individual fibers for preparation. Figure 5d shows a broken fiber with a core-mantel structure. The outer rim of the mantle (with a dented surface, seen in its lower part) contains some Al-Si, a small amount of K and possibly P (analyses 2 and 5); the inner rim shows only traces of Al-Si, but some U (analyses 3 and 4), whereas the center near to the channel (analyses 6) shows only the peaks of C-N-O, characteristic for OM. The count rate for O decreases systematically from outer rim to the center.

https://doi.org/10.5194/bg-2021-332
Preprint. Discussion started: 21 December 2021

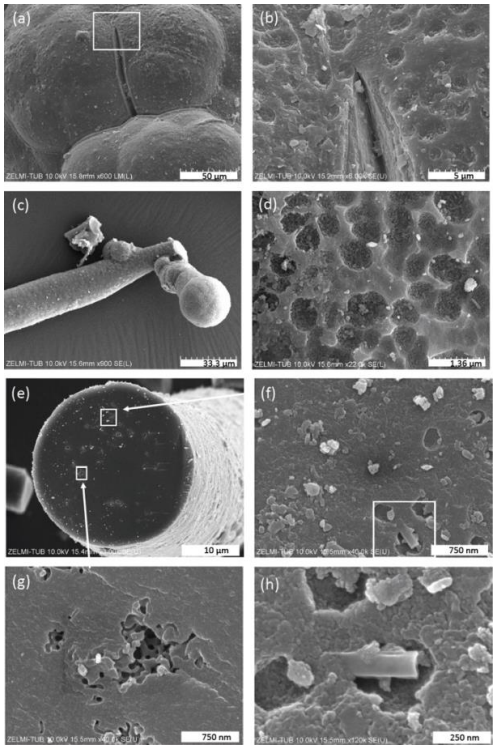

Figure 4: SEM images of surfaces of fossilized OM. (a) Botryoidal surface with a shrinking crack; inset shows enlarged part in (b) with a dented surface (sample #5). (c) Ball-shaped end of a fiber, with (d) dented surface (sample# 1). (e) Broken fiber (sample #3), showing internal porosity (f,g,h) with irregular outlines, of a few hundreds of nm wide. White rectangle in (f) indicates enlarged part shown in (h).

https://doi.org/10.5194/bg-2021-332
Preprint. Discussion started: 21 December 2021

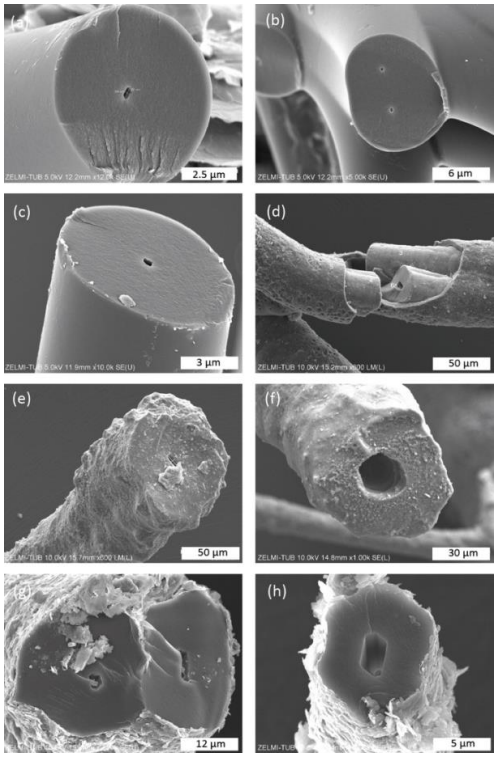

Figure 5: SEM images of broken fibers, showing a central channel. (a) Six-sided channel with dimensions 260 x 550 nm of fiber with a smooth surface, and fringe fractures on the broken face, indicating brittle behavior. (b) Double channel, probably initial crosscutting of a branching (cf. Fig. 2d). (c) Similar channel as in (a), but less regular outline (all sample #0). (d) Fiber with a core-mantle structure and a channel; numbers refer to analysis points (see text). Note dented surface in lower part of the mantle (sample #5). (e) Fiber with a rough surface and a channel 4 x 11 µm. (f) Large, ca. 25 µm wide channel with six-sided outline (both sample #5). (g,h) Fibers with encrustations of clay minerals and six-sided channels (sample #7).

2.2 Reflected light microscopy

In two-dimensional cuts in polished mounts in epoxy, observed under UV light for fluorescence and under white light for reflectivity (Fig. 6), the clear outer circular (to elliptical in oblique sections) shape of fibers is obvious in cross sections (Fig. 6a). In longitudinal sections (Fig. 6b), the symmetrical internal structure, which shows up in the cross sections, extends along the whole fiber. There are mainly three zones, an outer discontinuous, thin rim with a higher reflection/lower luminescence (zone 1), followed by a zone 2 with poorer reflection, higher

https://doi.org/10.5194/bg-2021-332
Preprint. Discussion started: 21 December 2021

238 fluorescence, and a core zone 3 with low fluorescence/intermediate reflectivity. The central,
239 open channel with different width is also seen in many fibers (Fig. 6a). Ball-shaped outgrowths
240 show the same type of zoning as the fibers. Flaky OM is seen as a thin (a few µm wide)
241 (bio?)film, intergrown with mineral matrix (Fig. 6c). Botryoidal shapes show difference in
242 reflectivity which runs parallel to the surface (Fig. 6d) and with highest reflectivity around
243 pores. Thick, irregularly shaped masses, possibly degraded OM (Fig. 6e,f) show rims high in
244 reflectance and zonal distribution of luminescence in UV light.

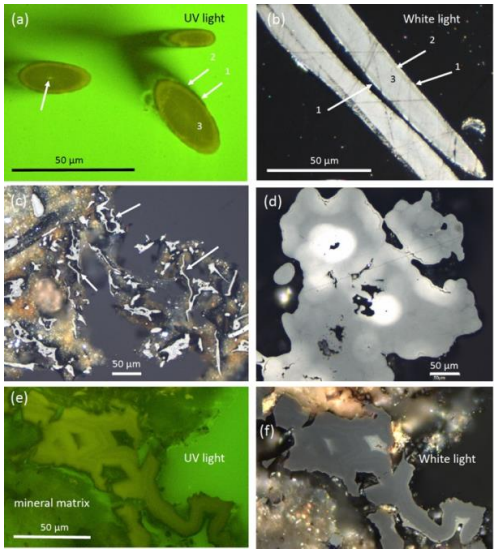

245

246 **Figure 6: Optical reflected light microscopy of polished grain mounts, under UV light for**
247 **fluorescence and under white light for reflectance. (a) Cross section of fibers, with a**
248 **central channel (left arrow) and three zones of fluorescence. (b) Longitudinal sections**
249 **show a symmetrical distribution of the three zones in reflectance, where the rim with high**
250 **reflectance corresponds to the rim with low fluorescence shown in (a). (c) Thin flaky OM,**
251 **interpreted as former biofilms (arrows). (d) Botryoidal OM with zonal distribution of**
252 **reflectivity. (e, f) Thick masses of flaky OM with zonal fluorescence and reflectivity.**

253

254

255 **2.3 Electron microprobe analyses (EMPA)**

256 The same mounts prepared for reflected light microscopy were used for EMPA. Within the
257 mineral matrix, we confirmed the presence of fluorite, closely intergrown with OM, and also

https://doi.org/10.5194/bg-2021-332
Preprint. Discussion started: 21 December 2021

identified buddingtonite, characterized by zoning and a significant decrease of the NH_4-component from core to rim (Fig. SI 2).

In order to show the distribution of elements in the OM by mapping with EMPA, we chose two cross sections of fibers (Fig. 7); the outer part of a large, segmented fiber (Fig. 8); a botryoidal part with ball-shaped outgrowths on more irregularly shaped OM; and the rim of flaky OM (Fig. 9). BSE images for location of the mapping areas in the selected grains are shown in the Fig. SI 3. Mapping included the characteristic elements identified before with SEM-EDS, i.e. O-N as part of the OM (C was not mapped because samples were C-coated), S and P, which can be part of the OM, but were also observed on the surface as sulfate or phosphate minerals (see above, SEM investigations), and Si, Al, and Ca as characteristic for silicates. Cl was mapped, because we found it also on the surface of the OM in the etch pits in EDS analysis, but was below detection level in the mappings. Because the OM is very sensitive to the electron beam (see image after mapping in Fig. SI 3c), we chose a trade-off between high resolution, X-ray excitation, and measuring time, but nevertheless, beam-related damage could not be completely avoided.

An oblique section of a 15 µm-wide fiber (Fig. 7) shows O enriched in the upper right part, where N and S are low, indicating simultaneous N and S loss during anaerobic oxidation. However, S is low in the area in the lower left with lowest BSE-contrast and where N is concentrated. Si and Al concentrated in the outer, irregular and discontinuous rim, together with O, present as Al-silicates as determined by SEM. The Ca-distribution is complex; it is enriched in the rim, but does not follow Si-Al. Instead, it forms an inner rim. It is also concentrated in the lower left part of this fiber, in the same area, where S is enriched. P shows some enrichments in spots in the inner part and in the rim, together with Ca interpreted as Ca-phosphate. Similar element distributions were observed in a circular section of a fiber (Fig. SI 4).

https://doi.org/10.5194/bg-2021-332
Preprint. Discussion started: 21 December 2021

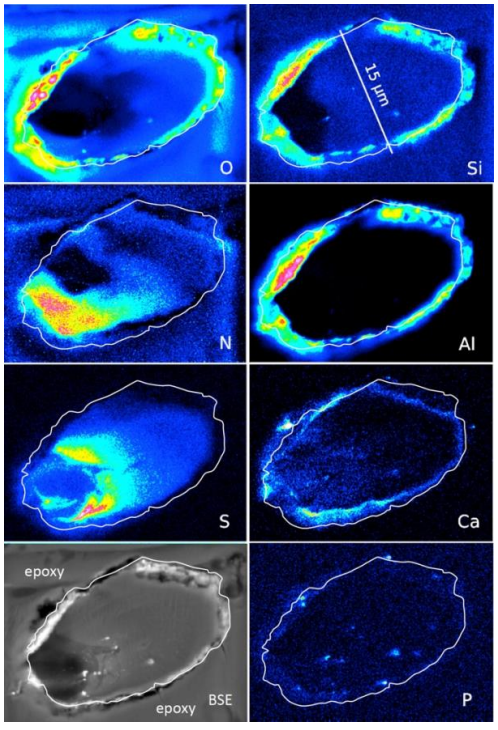

Figure 7: Element distribution (EMPA) of an oblique section of a 15 µm-wide fiber, embedded in epoxy. BSE-contrast is lowest in the area of low O, high N content. Si and Al (with O) form an outer rim, indicating Al-silicates (probably clay minerals, as determined by SEM). Ca is also concentrated in the rim, but also in spots together with P and in the area with high S. Scanning conditions: pixel resolution of 360 x 265, pixel size of 80 nm, dwell time per pixel of 200 ms, total scan area 28.8 x 21.2 µm.

The outer rim of a segmented fiber (Fig. 8) allows a sharper differentiation compared to the observations above: Si, Al, O are concentrated in the outer, irregular and discontinuous rim, together with Ca, which is enriched in spots together with P, but also with S (probably forming Ca-sulfate); S is enriched together with Ca in the outer rim. The outer rim is followed by an inner rim 1, poor in Ca, and then by an inner rim 2 with Ca-enrichment. O distribution is highest in the outer rim, high in the inner rim 1 with a rather sharp boundary to the inner rim 2, and then diffuse into the central part. N shows a relatively homogeneous distribution, but occurs up

https://doi.org/10.5194/bg-2021-332
Preprint. Discussion started: 21 December 2021

298 to the outer rim in areas of Si-Al concentrations, indicating the formation of NH_4-minerals
299 (buddingtonite, tobelite).

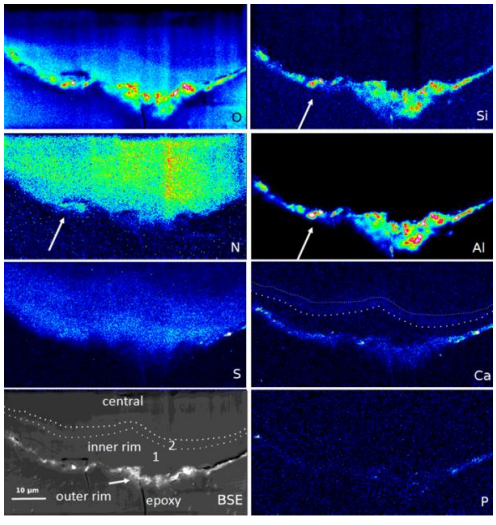

300

301 **Figure 8: Element distribution (EMPA) of the rim of a large fiber. The rim consists of**
302 **three areas, best visible in the BSE and Ca image: an outer, irregular and discontinuous**
303 **rim with enrichment of Si-Al-O and Ca, an inner rim 1, poor in Ca, followed by an**
304 **approximately 1-2 µm wide inner rim 2, enriched in Ca (dotted lines). In the outer rim,**
305 **Ca is also concentrated together with P and S. N distribution is relatively homogeneous,**
306 **but notably extends up to the outer rim, together with Al-Si (arrows), indicating**
307 **formation of NH_4-minerals (buddingtonite, tobelite). Vertical stripes are due to beam**
308 **damage. Scanning conditions: pixel resolution 350 x 180 with pixel size of 200 nm and a**
309 **dwell time per pixel of 200 ms, total scan area 70 x 36 µm.**

310

https://doi.org/10.5194/bg-2021-332
Preprint. Discussion started: 21 December 2021

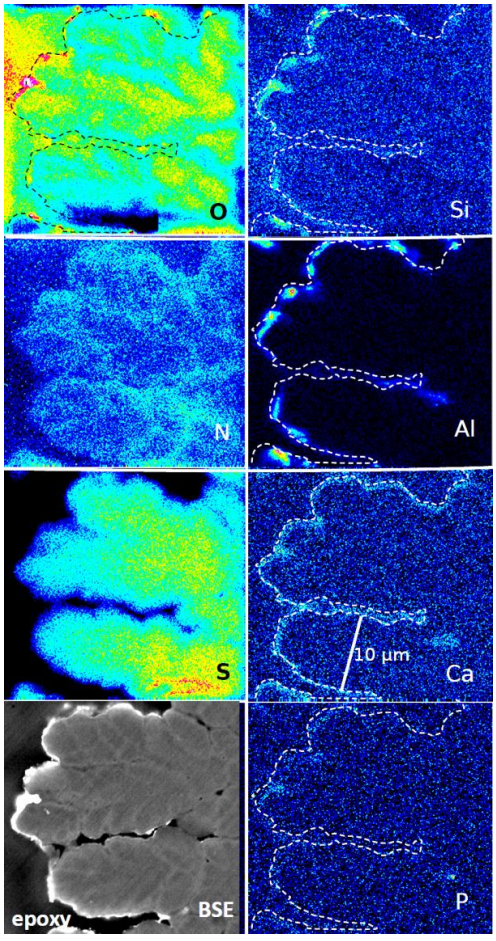

Figure 9: Element distribution (EMPA) in botryoidal OM. The rim (dashed line) is outlined as seen in the BSE image. Si, Al, and O are concentrated in a discontinuous rim, indicating Al-silicates. Ca is concentrated in spots in this rim together with P, indicating Ca-phosphate. Sulfur decreases systematically from the central part to the rim. N distribution is heterogeneous, and mimics the BSE contrast. Areas rich in N are poor in O. Scanning conditions: pixel resolution of 277 x 265 with pixel size of 120 nm and a dwell time per pixel of 200 ms, total scan area 33.2 x 31.8 µm.

https://doi.org/10.5194/bg-2021-332
Preprint. Discussion started: 21 December 2021

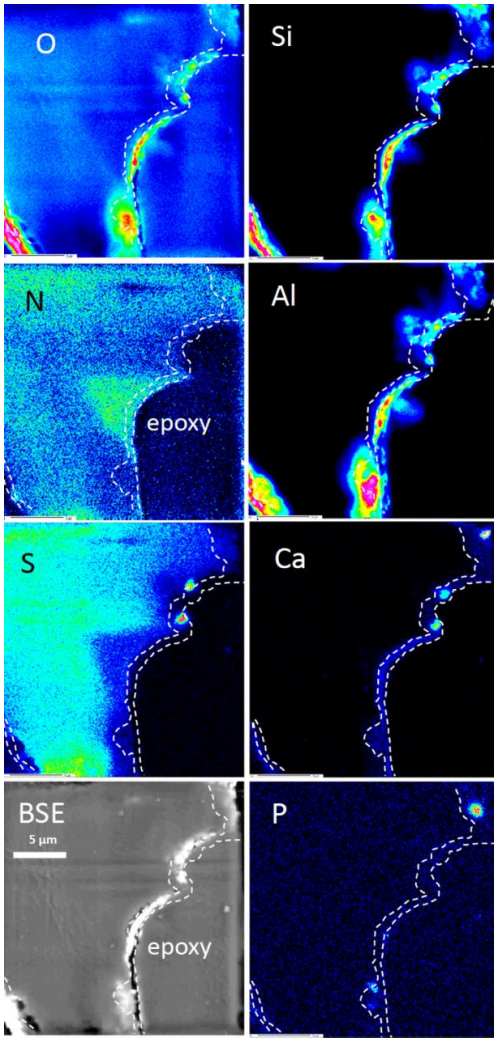

Figure 10: Element distribution (EMPA) of the rim of flaky OM. The rim is outlined as seen in the Ca image. Si, Al, and O are concentrated in a discontinuous rim, indicating Al-silicates. Ca is concentrated in spots together with P and S, indicating Ca-sulfates and Ca-phosphates, but also in a continuous rim with concentrations slightly above the background. Sulfur - except for the enrichment in spots - is absent in this area, and also less concentrated near to the rim. N distribution is heterogeneous, but as in Fig. 8 can extends up to the outer rim. Areas rich in N are poor in O.

The element distribution in botryoidal OM (Fig. 9) is characterized by an internal, heterogeneous N distribution, anticorrelated with O, which is visible in the BSE contrast. Sulfur systematically decreases from the central part towards the rim. Calcium is enriched in a thin

https://doi.org/10.5194/bg-2021-332
Preprint. Discussion started: 21 December 2021

rim, associated with P in a few spots as Ca-phosphate. The element distribution in flaky OM (Fig. 10) is generally similar to the observations made in fibers. Al-silicates form an outer, discontinuous rim, Ca is slightly above the background in the rim, but also forms discrete, small (≤ 1 µm) Ca-sulfates and Ca-phosphates. Sulfur is absent (except for the enrichment in Ca-sulfates) in this rim, indicating loss of S during maturation/fossilization. Towards the interior of the flaky OM, distribution of N, O, and S is heterogeneous, a possible indication for a primary (biological) character, combined with loss of N during thermal overprint. A different flaky object shows similar element distributions, however the phosphatization in the outermost rim is more pronounced than in the other mappings.

2.4 TEM investigations

TEM investigations of FIB-cut foils from a fiber, with the foil cut parallel to the elongation of the fiber. In the center (Fig. 11) it shows the amorphous character of the OM and the presence of Si together with C-N-O-S in the OM. In the rim, infiltration of Si, Al, and Ca, but in addition also Mg, Fe, K, and Ni in the whole fiber could be confirmed (Fig. SI 6); N was also confirmed by EELS analysis (Figure SI) in the dominantly C-rich matrix of the OM.

https://doi.org/10.5194/bg-2021-332
Preprint. Discussion started: 21 December 2021

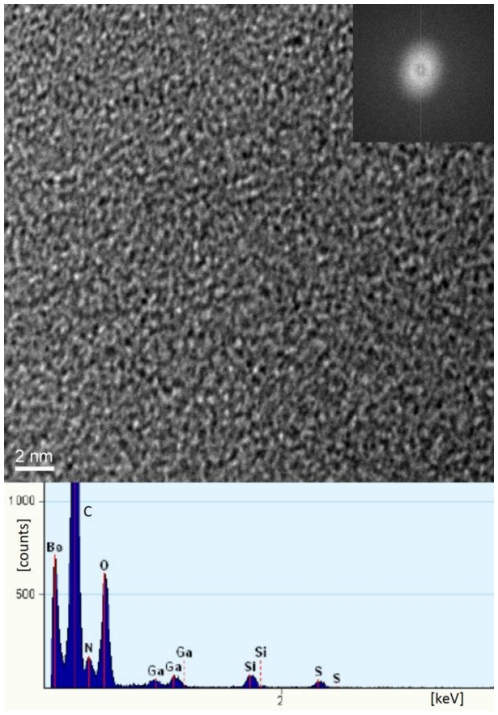

Figure 11: HRTEM-image of central part of a fiber, showing amorphous OM (inset is electron diffraction pattern) and EDS-spectrum of a spot, confirming Si as an impurity, C-N-O and S as the constituents of the OM. Ga-peak is from cutting of the FIB foil, Be is from the Be-sample holder.

2.5 Pyrolysis

Results of open-system pyrolysis are consistent with other observations, indicating mature or very mature OM, and there is no essential difference between samples with well-preserved shape and others with many incrustations. The gas chromatographic fingerprints of sample #0 are shown in Fig. 12, the results of the other samples are in Fig. SI 7. All are strongly dominated by hydrocarbon gases $C_{1\text{-}5}$ (methane through pentane) and subordinately by alkylated mono- and diaromatic compounds. These are typical pyrolysis breakdown products of already matured OM. The exact temperatures the material has experienced cannot be given as neither the chemical starting composition is known nor geological heating rates or heat flow. Nevertheless, the relatively high yield of compounds formed and the composition of the pyrolysate, especially

https://doi.org/10.5194/bg-2021-332
Preprint. Discussion started: 21 December 2021

363 presence of wet gases (C_{2-5}), indicates that the OM is not completely dead (graphite-like black
364 carbon), which is in line with a remaining fluorescence. Likely maximum geological
365 temperatures the OM has experienced a range between ~175 and ~200°C; in the case that peak
366 temperatures were very short-lived, temperatures could have been slightly higher, but the time
367 duration for the maturation of the Precambrian fossils is essentially unknown.

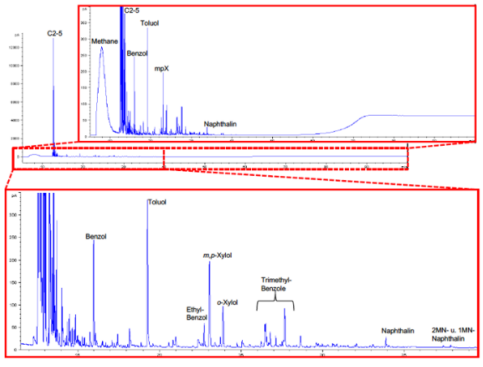

368

369 **Figure 12: Open-system pyrolysis GC-trace of sample #0/Museum Ac. Sci. Kyiv, is**
370 **dominated by hydrocarbon gases methane through pentane and subordinately by**
371 **alkylated mono- and diaromatic compounds, typical breakdown products of mature or**
372 **very mature OM.**

373

374 **2.6 U-Th-Pb analyses**

375 Table 2: Results of Pb isotope data of aliquots of OM, sample 9 (visually pure oxykerite) and
376 sample 1 (impure with whitish minerals)

sample	weight (g)	$^{206}Pb/^{204}Pb$	RSD%	$^{206}Pb/^{207}Pb$	RSD %	$^{208}Pb/^{204}Pb$	RSD%
UKR 1 9-a	0.00253	477.3	5.3	42.83	10.63	5.32	108.5
UKR 2 9-b	0.00090	36.46	3.5	17.04	2.132	2.01	42.46
UKR 3 9-c	0.00101	320.2	10.2	33.39	8.925	4.78	85.19
UKR 4 1-a	0.00038	51.00	0.9	18.45	2.753	1.61	70.18
UKR 5 1-b	0.00043	53.22	1.5	18.61	2.870	1.07	73.17
UKR 6 1-c	0.00067	47.43	0.9	18.01	2.634	1.41	64.14

377

https://doi.org/10.5194/bg-2021-332
Preprint. Discussion started: 21 December 2021

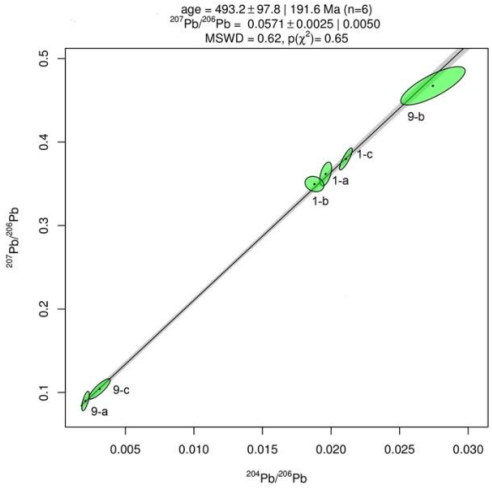

Figure 13: Results of Pb-Pb age determination of OM from Volyn pegmatite. The reference line corresponds to an age of 493.2 ± 97.8 Ma (1σ). The large uncertainty is mainly due to very small amounts of Pb in the samples, resulting in poor ion counting statistics in mass spectrometry. Data plotted and age calculated using the program Isoplot-R (Vermeesch, 2018).

Results of Pb isotope analyses of samples 9 and 1 and the OM from the pseudomorph sample are listed in Table 2 and shown in Fig. 13. The reference line corresponds to an age of 493.2 Ma, however with a large uncertainty of ± 97.8 Ma (1σ). The apparent age is considered as a minimum age, because OM is very susceptible for U, which is likely present in the fluids circulating in the pegmatitic environment since formation of the miarolitic chambers until modern times, a process that is capable to continuously reset U-Pb dates.

Chemical and U, Th, and Pb isotope data of black opal are presented in Tables SI 1, SI 2, and SI 3. Major element analyses (Table SI 1) in opal indicate approximately 2.5 wt% undetermined elements, likely H_2O and hydrocarbons. Minor elements are Al (up to 1 wt% Al_2O_3), Na, Ca, and Fe, which are present in 0.1 to 0.3 wt% oxide, whereas Ti, K, Mg, Fe, Cr, V, and Mn occur in smaller amounts. The heterogeneous distribution of elements is also seen in the trace element content among the three aliquots; Ba, Be, Li, Rb, Sc, Sr, Th, U, V, Zn, and Zr stand out with content each above 1 µg/g in some of the aliquots. The U-Th-Pb isotope data (Table SI 3)

https://doi.org/10.5194/bg-2021-332
Preprint. Discussion started: 21 December 2021

indicate open system behavior also for the black opal. The data show a large scatter; only two sample pairs allowed calculating old $^{208}Pb/^{232}Th$ ages of 1500±46 Ma and 1279±35 Ma, respectively.

3 Discussion

3.1 Fossilization process

A further determination of the exact nature of the excellently preserved microbial fossils requires a distinction between primary, i.e. biological, features and secondary, i.e. those produced by fossilization. The nature of the fossils (bacteria, archaea, or fungi), which colonized the igneous rocks, is not yet clarified; it will be done in a companion paper, also with more details on the spherical objects of OM.

The OM (kerite) is highly mature, as shown by pyrolysis experiments (Fig. 12), but not transformed into graphite, as shown by TEM investigations. It is completely amorphous (see in HRTEM image; Fig. 11), indicating rather low temperatures during fossilization and afterwards. This is also consistent with the observation that thin fibers are not completely opaque, but dark-brown transparent, confirming Luk'yanova et al.'s (1992) observations. Their X-ray data on the OM showed a diffuse maximum at c. 8 °θ, interpreted as a mixture of different carbohydrates with O, N, and S, some graphite-like sheets, hexamethylene and polymerized carbohydrates with O. The fringe fractures (Fig. 5a) show that the fiber behaved brittle, i.e. the whole fiber has reached a similarly high degree of aromatization, which relates to high thermal maturity.

Alteration of OM by anaerobic oxidation (e.g., the oxygen pattern along interfaces or affecting the whole kerite matrix) as a major feature is also seen in the element mapping (Figs. 7-10). Sulfur can form Ca-sulfates, as seen in µm-sized spots in the rim, but is generally decreased towards the rim; more detailed mapping of the element distribution in the outer rim area shows Ca enrichment in spots parallel with S, but also with P (Fig. 8), and we speculate about the

https://doi.org/10.5194/bg-2021-332
Preprint. Discussion started: 21 December 2021

423 presence of both, Ca-sulfate and Ca-phosphate nano-scale inclusions due to infiltration of Ca
424 and reaction with of S and P. S and P were transported out of the fiber and reaction with Ca
425 produced the Ca-free inner rim 1. Transport of Ca went further into the fiber producing the
426 inner rim 2. Phosphatization, a common fossilization process (e.g. Briggs, 2003) is thus only a
427 minor feature. Alternatively, the Ca distribution in the outer part of the fiber might mimic a
428 primary feature, preserved from their growth.

429 The distribution of Si-Al (together with O) is most conspicuous and restricted to a rim of ≈ 1 -
430 2 µm width (Figs. 7-11). The presence of Si-Al is confirmed by analytical data with SEM (Fig.
431 5d) and TEM (Fig. 11), and suggests that silicification is the first-order process of fossilization.
432 The patchy distribution indicates the formation of Al-silicate minerals, probably kaolinite or
433 related phases. These patches were observed on the surface of the fibers as vermicular structures
434 (Fig. 3c), some with clear development of crystal faces (Fig. 3a) and continue into more coarse-
435 grained features, which we call encrustations (Fig. 3d). Finally, the patches change into
436 intergrowths of minerals, which could be characterized by shape and chemistry as alkali-
437 feldspar, clay minerals, opal, Fe-sulfides, and fluorite (Fig. 3e-h).

438 The porosity observed on the surface of botryoidal structures and ball-shaped outgrowths on
439 fibers (Fig. 4c,d) and on a broken cross section (Fig. 4e-h) are interpreted as degassing features.
440 The irregular internal pores on the scale of a few hundred nanometers indicate irregular
441 pathways of the gas, transitional towards the outer part of the OM into more regular, circular
442 and larger pores of 1 to 2 µm in diameter. Cracks in the surface (Fig. 4a,b) are interpreted as a
443 shrinking phenomenon in the OM, and the irregular shape of flaky OM on the etch pits of beryl
444 (Fig. 2a,c) is also interpreted as a shrinking phenomenon of a formerly coherent biofilm. The
445 outgrowths and ball-shaped ends of fibers were interpreted by Zhmur (2003) as spherical
446 swellings of the fiber sheaths produced by degassing. However, their size and transition to
447 botryoidal and dented structures (Fig. 4) is more consistent with an interpretation as a primary

https://doi.org/10.5194/bg-2021-332
Preprint. Discussion started: 21 December 2021

448 feature. In addition, the cross sections (Fig. 6) of these structures with regular outline of e.g.
449 the distribution of fluorescence and the mappings (Fig. 9) also indicate a primary feature. In
450 contrast, the more irregular, ridge-like features (Fig. 2d), covered with platy clay minerals such
451 as kaolinite (Figs. 2, 5g,h), seem to represent strongly modified, original segmentation of the
452 fibers during the fossilization process.

453 Many, but not all of the broken fibers show a central cavity (Fig. 5), visible also in BSE images
454 of embedded fibers in cross sections, and it is the question if this is a primary or a secondary
455 fossilization feature. In small nanometer-scale cavities, the ratio of the solid outer part to cavity
456 is ≈ 10:1 (in cross section, see Fig. 5a,c), and together with the observation that not all fibers
457 have this cavity, it might be interpreted as a shrinking phenomenon. However, in µm-sized
458 cavities the ratio goes down to ≈ 1:1 (Fig. 5f,h), and such a high loss of material during
459 degassing seems unlikely. Furthermore, the six-sided outline, seen in small and large cavities,
460 cannot be explained by shrinking. There is no reason why a cylindrical body during shrinking
461 should open a central cavity with a regular outline.

462 In order to describe the infiltration process for the fossilization and the responsible fluid phase,
463 it is important to note that OM occurs not only with the well-preserved morphology described
464 above, but also in patches of highly degraded OM, as shown in the previous description of a
465 breccia from these pegmatites (Franz et al., 2017). This OM is not only highly oxygenated (with
466 up to 40 atom% of O), but is also enriched in F (≤ 1.7 atom%), Zr (≤ 7 atom%), Sc (≤ 0.8
467 atom%), Y (≤ 2.7 atom%), and REE (sum ≤ 0.35 atom%), elements that were most probably
468 derived from the pegmatitic environment.

469 What is striking in all observations is the close connection between OM and fluorite, which was
470 also described by Zhmur (2003). The whole occurrence in the granitic pegmatites with a large
471 amount of topaz in the chambers (Lyckberg et al., 2019, report that a single pegmatite, no. 464,
472 had produced 6 tons topaz in mining) points to a high concentration of F in the late-magmatic

https://doi.org/10.5194/bg-2021-332
Preprint. Discussion started: 21 December 2021

473 to hydrothermal fluids. In addition, we observed F-rich muscovite during the formation of the
474 breccia (Franz et al., 2017) and this also points to the importance of F-activity. This fluid likely
475 carried a high amount of silica as SiF_4 (plus other components, such as Al, alkalies, Ca, Mg,
476 and Fe).

477 For the fossilization process we assume that this fluid was able to react with the OM in a depth
478 of 1-2 µm (Figs. 7-10). Gorlenko et al. (2000) and Zhmur (2003) described the outer part of
479 the fibers as a former sheath of the microorganisms. We interpreted this rim area as a former
480 thin coating of biofilm that was probably very sensitive in a first stage of Si-Al-infiltration, with
481 Ca-infiltration slightly deeper into the OM. The small mineralized structures on the surface of
482 fibers (Fig. 3c) resemble what Gorlenko et al. (2000) interpreted as membrane leaflets (their
483 Fig. 2).

484 **3.2 Environment of fossilization**

485 The geological situation for the fossilization is summarized in Figure 14. We assume that
486 fossilization must have occurred during a hydrothermal event within a fluid that carried enough
487 Si, Al, F, and Ca to react with the degradation products of the OM in nano-environments. The
488 Korosten pluton intruded into continental crust, and the geological situation indicates a long-
489 living plutonic-volcanic activity (Shumlyanskyy et al., 2021), likely with near-surface geyser
490 systems. The crystallization of the pegmatites and formation of the chambers occurred in a
491 depth of 2 to 2.5 km (Lukashev, 1976, Kalyuzhnyi et al., 1971; Voznyak et al., 2007). The
492 miarolitic cavities of the granite, possibly with periodical influx of hydrothermal waters,
493 provided the space for a continental deep biosphere, consisting probably of anoxic,
494 thermophilic and acidophilic microbial species. Methanogenic bacteria (indicated by C and N
495 stable isotopes; Franz et al., 2017) might have been an important part of such a cryptic
496 endolithic micro-ecosystem in a continental, terrestrial environment.

https://doi.org/10.5194/bg-2021-332
Preprint. Discussion started: 21 December 2021

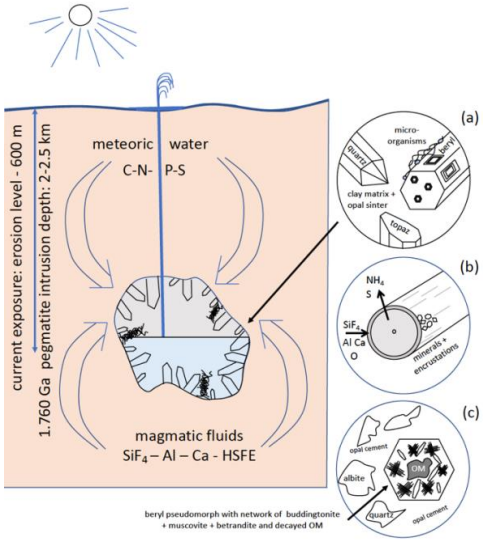

497

498 **Figure 14: Schematic illustration of the geological environment of pegmatites of the**
499 **Korosten pluton, Ukraine, with m-sized miarolitic chambers and a near-surface geyser**
500 **system. The chambers provided the space for an endolithic micro-ecosystem, which**
501 **consists (a) of three morphologically different organisms (fibrous, flaky, and rare**
502 **spherical OM), attached to the pegmatitic minerals, also in etch pits of beryl. (b)**
503 **Fossilization occurs due to influx of hydrothermal fluids, carrying SiF_4 and starts with a**
504 **µm-thin layer of Al-Si enrichment, which develops into clay minerals, feldspar, and finally**
505 **into encrustations. (c) OM is found also in breccias, formed during collapse of some**
506 **chambers, where it is strongly decayed, providing NH_4 for the formation of buddingtonite,**
507 **together with muscovite and bertrandite, in pseudomorphs after beryl.**

508

509 The flaky OM, also visible as thin films in cross section, point to the participation of biofilms
510 in this ecosystem, which might have developed as soon as the temperatures in the miarolitic
511 chambers were sufficiently low for organisms. The essential components for the organisms -
512 C, N, S, P - or the microorganisms themselves were transported with meteoric water from the
513 surface to the chambers. Alternatively, the components for the organisms might have been
514 transported from the metamorphic country rocks of the Korosten pluton into the chambers via
515 hydrothermal convection cells (e.g. Bobos and Williams, 2017, who described NH_4-transport
516 for tobelite formation in a sedimentary basin).

https://doi.org/10.5194/bg-2021-332
Preprint. Discussion started: 21 December 2021

517 Some of the miarolitic cavities collapsed and produced a breccia, which also contains degraded
518 OM and black opal with inclusion of carbohydrates (Franz et al., 2017). Chambers, which did
519 not collapse, must have been sealed. They contained a large amount of gas under high pressure,
520 and the sealing preserved the gas from escape. Lyckberg et al. (2019) reported that old log
521 books of the mining activities in Volyn describe an event in 1955, when at a depth of 600 m
522 drilling penetrated a gas-filled cavity, and as a consequence the entire drill steel shot out of the
523 hole and toppled the drill tower. It took more than 30 min, before the highly pressurized gas
524 slowed down. That a large amount of gas must have been produced during decay of the OM is
525 also indicated by the fluid-solid equilibria between NH_4^+ and K^+, responsible for the
526 buddingtonite formation. It is known from experimental data that for the transformation of K-
527 feldspar into buddingtonite, X_{NH4} in the fluid must be very high (Pöter et al., 2004).

528 Laser-ablation dating with the $^{39}Ar/^{40}Ar$ method of the muscovite from the breccia yielded an
529 age of 1491±9 Ma (MSWD 0.98), interpreted as the age of the hydrothermal breccia formation
530 (Franz et al., in press). Analyses of buddingtonite yielded an age range from 383±12 Ma to
531 563±14 Ma, and the oldest age of 563 Ma is interpreted as a minimum age, because of probable
532 Ar-loss of the very fine-grained buddingtonite crystals. This minimum age is in the same range
533 as the results of our attempt to date the fossils directly with Pb-Pb-dating (Fig. 11). The
534 maximum age is given by the intrusion age of the pegmatites, 1760±3 Ma (Fig. 1;
535 Shumlyanksyy et al., 2021). The intrusion depth of 2 to 2.5 km might have been the depth for
536 the microbial community, but there is a significant time lag between pegmatite formation (1.76
537 Ga) and the formation of the breccia (c. 1.49 Ga) during which exhumation could have
538 occurred.

539 Silicification of microbial organisms is typical for geyser systems, as shown by many recent
540 analogues, e.g. for Yellowstone, USA (Cady and Farmer, 1996), Waiotapu, New Zealand
541 (Handley et al., 2008) and others (see references in Alleon et al, 2016). Consequently, a number

https://doi.org/10.5194/bg-2021-332
Preprint. Discussion started: 21 December 2021

542 of experimental studies on silicification of microorganisms including the processes of silica
543 polymerization and precipitation in the presence of microorganisms was undertaken, starting
544 with the earliest work by Oehler (1976). Experimental silicification of Archaea (Orange et al.,
545 2009) has shown that the outer surface layer of these organisms is the site for incipient
546 silicification, and the ubiquity of biofilms on surfaces in hot-springs (e.g. Cady and Farmer,
547 1996; Handley et al., 2008; Kremer et al., 2012) and other environments (Bortnikov et al., 2012)
548 indicates potential presence of biofilms also in the Precambrian at the subvolcanic geyser
549 system in the Korosten pluton. Extracellular polymeric substances play an important role in
550 silicification and fossilization as shown by many authors (see references above, and therein),
551 and fossilization of biofilms occurs very rapidly (Rozanov, 2003). After silicification of
552 extracellular polymeric substances, clay minerals developed on the surface of the OM in the
553 fossils from Volyn. This phenomenon was also observed in experimental studies (Urrutia and
554 Beveridge, 1994) and in natural environments (Kremer et al., 2012; Bortnikov et al., 2012).

555 The formation of the 1-2 μm thick layer of Si-Al infiltration and development of encrustations
556 of Al-silicates was essential for the excellent preservation of the morphology of the
557 microfossils. The fossilization of soft tissue organisms requires special conditions, which
558 prevent autolysis. In fossilization experiments of crustacean eggs with phosphoric acid, Hippler
559 et al. (2012) pointed out that rapid heating before treatment with phosphoric acid was essential
560 for perfect preservation of the morphology of OM. This treatment denaturized the proteins of
561 the crustacean eggs, creating a stable template for mineralization, which occurred rapidly within
562 one to two weeks. We suspect a similar process for the silicification process at the Volyn
563 locality. Anaerobic conditions in the deep biosphere prevented early autolysis of the organisms,
564 then shock heating might have occurred due to influx of hot hydrothermal waters into the
565 miarolitic caves, carrying SiF_4 together with Al, Ca, and other elements, producing rapid
566 infiltration of Si, Al, and Ca into the outer surface layer of the organisms, including
567 precipitation of opal (Fig. 3f). The early envelope of silicification minimizes the molecular

https://doi.org/10.5194/bg-2021-332
Preprint. Discussion started: 21 December 2021

568 degradation of the OM, as also shown experimentally by Alleon et al. (2016). Further heating
569 (without deformation) after formation of the Si-Al enriched outer rim enhanced the decay of
570 the OM, but did not destroy the morphology. Kremer at al. (2012) pointed out that the
571 morphology of calcified cyanobacteria was destroyed, whereas silicification, when rapid, helps
572 to preserve their morphological details. That fossilization of bacterial organisms is a rapid
573 process has also been postulated by Rozanov (2003). Raff et al. (2008) demonstrated
574 experimentally that under anaerobic conditions (preventing autolysis) rapid formation of
575 bacterially induced biofilms on the surface of organisms provided the site for early
576 mineralization with Ca-minerals. These biofilm bacteria induce a catalyzing process for rapid
577 fine-grained mineralization, which was also postulated by Briggs (2003). Extracellular
578 polymeric substances are known to provoke diagenetic mineralization, possibly as the result of
579 liberation of adsorbed cations during degradation (Arp et al., 1999; Dupraz and Visscher, 2005;
580 Altermann et al., 2006). Notably, most of the cases described in the literature and quoted above
581 deal with marine environments, whereas the case reported here deals with a Precambrian
582 continental environment.

583 Extracellular biosilicification capability of bacteria and archaea in geothermal environments
584 with transformation of soluble $Si(OH)_4$ into nano-scale SiO_2 precipitates on the surface has
585 recently been emphasized by Ikeda (2021). Bacteria, such as *Thermus thermophilus* (Iwai et
586 al., 2010), can form siliceous deposits from supersaturated solutions in biofilms on the outer
587 surface layer of the cell envelope.

588 Zhmur (2003), based on the data by Gorlenko et al. (2000) and by comparison with other
589 occurrences of OM in igneous rocks and in recent geyser environments, proposed a
590 hydrothermal origin of cyanobacteria and microbial bio-mats in geyser ponds for the Volyn
591 occurrence. The fossilization occurred in situ in zones of silica precipitation, forming sealed
592 cup-like structures. The floating cyanobacterial mat was buried in the self-sealed biogenic-

https://doi.org/10.5194/bg-2021-332
Preprint. Discussion started: 21 December 2021

geyser structure that was formed at the hydrothermal discharge site, and collapse of these structures produced the breccia, observed at the Volyn deposit. This model implies that the fossils were transported downward with the geyser water to the chambers. This is not consistent with our observations, which show that the fibers, together with irregular and spherical OM grew onto and into the etch pits of beryl (Fig. 2a). If transport had occurred, this would have probably destroyed the delicate fibers, producing a mat-like OM, such as described by Zhmur (2003; his Fig. 1).

4 Concluding remarks

The pegmatitic Volyn kerite occurrence is probably one of the localities world-wide with the best preserved Precambrian soft tissue fossils. Common occurrences of (Precambrian) fossils are in sediments, especially in chert, but there is more and more evidence of OM in the pore space of igneous rocks (Ivarsson et al., 2020). Several factors have contributed to the micro-taphonomical process to preserve the Volyn fossils as part of an endolithic micro-ecosystem. First, the chambers in the pegmatites provided an exceptionally large 'pore' space. Secondly, water was present in such an environment, necessary for life, although this was not necessarily a completely water-filled cave, but possibly a cave with temporary changes in the water level. Transport of Si was likely enhanced by F, present in this pegmatitic, granitic environment. OM would have decayed, when O was available, hence silicification of the outer parts of the kerite fossils implies rapid reaction with Si and shielding for access of O. This environment in the deep biosphere was similar to geyser systems, which are known to be sites of preferred microbial growth. The microorganisms contribute to the microstructural development of geyserites by providing a favored substrate for opaline silica precipitation, and encrustation and degradation of microorganisms is the dominant mode of fossilization at the high temperature end of the geyser system (Cady and Farmer, 1996).

https://doi.org/10.5194/bg-2021-332
Preprint. Discussion started: 21 December 2021

There is growing awareness of the importance of life in the deep igneous biosphere especially in the record of early life, the most important reservoir of biomass in the Precambrian (Ivarsson et al. 2020). The presence of F-rich hydrothermal waters in the late stage of granitic, subvolcanic plutons might be a common scenario for preservation of microorganisms, without the later influence of deformation and metamorphism, such as in chert, where most of the studies of Precambrian fossils has been undertaken. Granitic rocks might be sites for the very early diagenetic emplacement of silica, leading to 3D preservation of non-biomineralizing fossils, the "Bitter Springs-type preservation" (Butterfield, 2003). The search for indications for early life, and its evolution during the Precambrian has concentrated mainly on submarine hydrothermal vents (e.g. Dodd et al., 2017), but it should be extended also to terrestrial environments.

Acknowledgements

We thank A. Schreiber for preparation of FIB foils and D. Hippler for comments on an earlier version. (reviews, editorial handling)

Author contributions: GF (concept, writing), PL (sampling, reviewing), VC (sampling), VK (sampling), H-MS (reviewing, reflected light microscopy), NM (pyrolysis), RW (TEM), JG (U-Th-Pb), UG (SEM), JN (EMPA)

https://doi.org/10.5194/bg-2021-332
Preprint. Discussion started: 21 December 2021

638 **References**

639 Alleon, J., Bernard, S., Le Guillou, C., Daval, D., Skouri-Panet, F., Pont, S., Delbes., and
640 Robert, F.: Early entombment within silica minimizes the molecular degradation of
641 microorganisms during advanced diagenesis, Chem. Geol., 437, 98-108, 2016.

642 Altermann, W., Kazmierczak, J., Oren, A., and Wright, D. T.: Cyanobacterial calcification and
643 its rock-building potential during 3.5 billion years of Earth history, Geobiology, 4,147–166,
644 2006.

645 Arp, G., Reimer, A., Reitner, J.: Calcification in cyanobacterial biofilms of alkaline salt

646 Lakes, Eur. J. Phycol., 34, 393–403, 1999.

647 Butterfield, N. J.: Exceptional fossil preservation and the Cambrian explosion, Integr. Compar.
648 Biol., 43, 166-177, 2003.

649 Bobos, I., and Williams, L. B.: Boron, lithium and nitrogen isotope geochemistry of NH_4-illite
650 clays in the fossil hydrothermal system of Harghita Bãi, East Carpathians, Romania, Chem.
651 Geol., 473, 22-39, 2017.

652 Bortnikov, N. S., Novikov, V. M., Soboleva, S. V., Savko, A. D., Boeva, N. M., Zhegallo, E.
653 A., and Bushueva, E. B.: The role of organic matter in the formation of fireproof clay of the
654 Latnenskoe Deposit, Dokl. Earth Sci., 444, No. 1, 634-639, 2012.

655 Briggs, D. E. G.: The role of decay and mineralization in the preservation of soft-bodied fossils,
656 Annu. Rev. Earth Planet. Sci., 31, 275–301, 2003.

657 Cady, S. L., and Farmer, J. D.: Fossilization processes in siliceous thermal springs: trends in
658 preservation along thermal gradients, Evolution of hydrothermal ecosystems on Earth and
659 Mars? Chichester (Ciba Foundation Symposium), Wiley, 202, 150-173, 1996.

660 Dodd, M. S., Papineau, D., Grenne, T., Slack, J. F., Rittner, M., Pirajno, F., O'Neill, J., and
661 Little, C. T.: Evidence for early life in Earth's oldest hydrothermal vent precipitates, Nature,
662 543(7643), 60-64, 2017.

663 Dupraz, C., Visscher, P. T.: Microbial lithification in marine stromatolites and hypersaline
664 mats, Trends Microbiol. 13, 429–438, 2005.

665 Franz, G., V. Khomenko, Vishnyevskyy, A., Wirth, R., Struck, U., Nissen, J., Gernert, U., and
666 Rocholl, A.: Biologically mediated crystallization of buddingtonite in the Paleoproterozoic:
667 Organic-igneous interactions from the Volyn pegmatite, Ukraine, Amer. Mineral., 10, 2119-
668 2135, 2017.

669 Franz, G., Sudo, M., Khomenko, V. (in revision): $^{40}Ar/^{39}Ar$ dating of a hydrothermal pegmatitic
670 buddingtonite-muscovite assemblage from Volyn, Ukraine, Eur. J. Mineral.

671 Ginzburg, A.I., Bulgakov, V.S., Vasilishin, I.S., Luk'yanova, V.T., Solntseva, L.S., Urmenova,
672 A.M., and Uspenskaya, V.A.: Kerite from pegmatites of Volyn, Dokl. Akad. Nauk SSSR, 292,
673 188–191, 1987, (in Russian).

674 Gorlenko, V.M., Zhmur, S.I., Duda, V.I., Osipov, G.A., Suzina, N.E., and Dmitriev, V. V.: Fine
675 structure of fossilized bacteria in Volyn kerite, Origin of Life and Evolution of the Biosphere,
676 30, 567–577, 2000.

677 Handley, K. M., Turner, S. J., Campbell, K. A., and Mountain, B. W.: Silicifying biofilm
678 exopolymers on a hot-spring microstromatolite: templating nanometer-thick laminae,
679 Astrobiol., 8(4), 747-770, 2008.

https://doi.org/10.5194/bg-2021-332
Preprint. Discussion started: 21 December 2021

680 Hippler, D., Hu, N., Steiner, M., Scholtz, G., and Franz, G.: Experimental mineralization of
681 crustacean eggs: new implications for the fossilization of Precambrian–Cambrian embryos,
682 Biogeosci., 9(5), 1765-1775, 2012.

683 Ikeda, T.: Bacterial biosilicification: a new insight into the global silicon cycle, Biosci.,
684 Biotechn., Biochem., 85, 6, 1324-1331, 2021.

685 Ivanovich, P. V., and Alekseevich, D. S.: Mineralogy of the Volynian chamber pegmatites,
686 EKOST Association, Mineral. Almanac, 12, 128 p, Moscow, 2007.

687 Ivarsson, M., Drake, H., Neubeck, A., Sallstedt, T., Bengtson, S., Roberts, N. M. W., and
688 Rasmussen, B.: The fossil record of igneous rocks, Earth Sci. Rev., 210, 2020.

689 Iwai, S., Doi, K., Fujino, Y., Nakazono, T., Fukuda, K., Motomura, Y., and Ogata, S.: Silica
690 deposition and phenotypic changes to *Thermus thermophilus* cultivated in the presence of
691 supersaturated silicia, The ISME J. 4, 809–816, 2021.

692 Kalyuzhnyi V. A., Voznyak, D. K., Gigashvili, G. M.: Mineral-forming fluids and mineral
693 paragenesis of chamber pegmatites of Ukraine, Kyiv: Naukova Dumka, 216 pp., 1971 (in
694 Ukrainian).

695 Kremer, B., Kazmierczak, J., Lukomska-Kowalczyk, M., and Kempe, S.: Calcification and
696 silicification: fossilization potential of cyanobacteria from stromatolites of Niuafo'ou's Caldera
697 Lakes (Tonga) and implications for the early fossil record, Astrobiol. 12(6), 535-548, 2012.

698 Lukashev, A. N.: Depth of pegmatite formation, Moscow, Nedra, 152 pp., 1976, (in Russian).

699 Lu'kyanova, V. T., Lobzova, R. V., and Popov, V. T.: Filaceous kerite in pegmatites of Volyn,
700 Izvest. Ross. Akad. Nauk Ser. Geologicheskaya, 5, 102–118, 1992 (in Russian).

701 Lyckberg, P., Chernousenko, V., and Wilson, W. E.: Famous mineral localities: Volodarsk-
702 Volynski, Zhitomir Oblast, Ukraine, The Mineral. Record 40, 473-506, 2009.

703 Lyckberg, P., Chournousenko, V., and Chournousenko, O.: Giant heliodor and topaz pockets
704 of the Volodarsk chamber pegmatites, Korosten pluton, Ukraine, 36th Intern. Gemm. Conf..
705 Nantes, France, Abstr. vol., 78-83, 2019.

706 Oehler, J.H.: Experimental studies in Precambrian paleontology: structural and chemical
707 changes in blue-green algae during simulated fossilization in synthetic chert, Geol. Soc. Am.
708 Bull. 87 (1), 117–129, 1976.

709 Orange, F., Westall, F., Disnar, J. R., Prieur, D., Bienvenu, N., Le Romancer, M., and Défarge,
710 C.: Experimental silicification of the extremophilic Archaea Pyrococcus abyssi and
711 Methanocaldococcus jannaschii: applications in the search for evidence of life in early Earth
712 and extraterrestrial rocks, Geobiol., 7(4), 403-418, 2009.

713 Pöter, B., Gottschalk, M., and Heinrich, W.: Experimental determination of ammonium
714 partitioning among muscovite, K-feldspar, and aqueous chloride solutions, Lithos, 74, 67–90,
715 2004.

716 Raff, E. C., Schollaert, K. L., Nelson, D. E., Donoghue, P. C., Thomas, C. W., Turner, F. R., ...
717 and Raff, R. A.: Embryo fossilization is a biological process mediated by microbial biofilms,
718 Proc. Nat. Acad. Sci., 105(49), 19360-19365, 2008.

719 Rozanov, A. Yu.: Fossil bacteria, sedimentogenesis, and the early biospheric evolution,
720 Paleontol. Zh., No. 6, 41–49, 2003, [Paleontol. J. 37 (6), 600–608 (2003)].

721 Shumlyanskyy, L., Belousoca, E., and Petrenko, O.: Geochemistry of zircons from basic rocks
722 of the Korosten anorthosite-mangerite-charnockite-granite complex, northwestern region of the
723 Ukranian Shield, Mineral. Petrol., 111(4), 459-466, 2017.

https://doi.org/10.5194/bg-2021-332
Preprint. Discussion started: 21 December 2021

724 Shumlyanskyy, L., Franz, G., Glynn, S., Spencer, C., Mytrokhyn, O., Voznyak, D., and Bilan
725 O.: Geochronology of granites of the western part of the Korosten AMCG complex (Ukrainian
726 Shield): implications for the emplacement history and origin of miarolitic pegmatites, Eur. J.
727 Min., 33, 703, 2021.

728 Urrutia, M. M., and Beveridge, T. J.: Formation of fine-grained metal and silicate precipitates
729 on a bacterial surface (Bacillus subtilis), Chem. Geol., 116(3-4), 261-280, 1994.

730 Vermeesch, P.: IsoplotR: a free and open toolbox for geochronology, Geosci. Front., 9, 1479-
731 1493, 2018 doi: 10.1016/j.gsf.2018.04.001.

732 Voznyak, D.K., Khomenko, V.M., Franz, G., and Wiedenbeck, M. Physico-chemical
733 conditions of the late stage of Volyn pegmatite evolution: Fluid inclusions in beryl studied by
734 thermobarometry and IR-spectroscopy methods, Mineral. J. (Ukraine), 34, 26–38, 2012 (in
735 Ukrainian).

736 Zhmur, S. I.: Origin of Cambrian fibrous kerites of the Volyn region, Lithol. Mineral Resour.,
737 38, 55-73, 2003.